www.nature.com/scientificdata

scientific data

OPEN

DATA DESCRIPTOR

Dataset of power, wind and acoustic measurements from wind tunnel tests on a small Savonius wind turbine

Luisa Pagnini[1] ✉, Piotr Doerffer[2], Joanna Grzelak[2], Józef Kotus[3], Giuseppe Piccardo[1], Maria Pia Repetto[1] & Krzysztof Doerffer[2]

This paper presents a publicly available dataset from wind tunnel experiments carried out under the European Project ERIES (Engineering Research Infrastructures for European Synergies) at the Giovanni Solari Wind Tunnel of the University of Genoa. The dataset contains synchronized measurements acquired on a small-diameter, high-rotational-speed Savonius wind turbine under controlled laboratory conditions. Experiments were performed for wind tunnel velocities up to 21 m/s and rotor speeds up to 2500 rpm, under both smooth and turbulent flow conditions, with turbulence intensities of approximately 4% and 8%. The dataset includes: the inlet wind speed measured by a Pitot-static tube; the undisturbed wind speed, measured by a Cobra probe; the rotor's rotational velocity, measured by Hall sensors; generated power, estimated from the generated current and rotational velocity; the upstream and downstream flow velocities, recorded by hot wires. Additionally, noise emissions were recorded by four microphones downstream, providing insight into a relatively unexplored aspect of wind turbine performance in the literature.

Background & Summary

Wind turbines, especially those of small size, show significant potential for integration into urban environments, offering a promising solution for distributed energy generation[1]. In densely populated areas, where energy demands are high, local energy production is becoming more and more popular having the advantage of exploiting renewable sources and positively impacting on social perception[2,3]. Small wind turbines are not yet as competitive as other renewable options, such as solar power or large-scale wind farms, due to higher costs per unit of energy, lower efficiency, and less widespread adoption[4,5]. However, they can contribute to meeting the growing demand, either in isolated contexts, integrated with other renewable energy systems[6], or by supplying distributed energy production through numerous small wind turbines[7–9]. Regrettably, small wind turbines are typically situated in areas with low to moderate wind speeds, prioritizing locations where energy demand is high over those with optimal wind conditions[10,11]. Moreover, the high rotational speeds of these devices, combined with their proximity to residential areas, can make the resulting noise particularly disruptive[12]. Beyond the audible disturbance, the visual impact of the turbines has been shown to heighten perceived annoyance, compounding the overall negative experience[13].

Industrial facilities and urban infrastructures offer numerous sites where wind speeds are accelerated, presenting opportunities for installing small wind turbines without the need for additional supports[14] This approach significantly reduces installation costs compared to conventional setups, as turbines can be mounted on existing structures like bridges and buildings[15,16], capitalizing on favorable wind conditions. However, such settings are prone to strong wind gusts, and localized obstacles can create high-wind zones, necessitating periodic turbine shutdowns for safety[17,18].

[1]Dept of Civil, Chemical and Environmental Engineering, University of Genova, Genoa, Italy. [2]Faculty of Mechnical Engineering and Ship Technology, Gdańsk University of Technology, Gdańsk, Poland. [3]Multimedia Systems Department, Faculty of Electronics, Telecommunications and Informatics, Gdańsk University of Technology, Gdańsk, Poland. ✉e-mail: luisa.pagnini@unige.it

Savonius-type wind turbines have been in existence for over a century, with extensive research dedicated to their development[19,20] through wind tunnel tests and/or CFD simulations. A comprehensive programme of wind tunnel experiments and modelling analyses on two-bladed Savonius rotors explored geometric parameters to optimise the rotor configuration and improve its efficiency[21]. Other studies investigated the aerodynamic performance of single-, two-, and three-stage systems[22,23] and examined various geometric parameters[24], including the number of blades[25]. Several enhanced configurations have been explored to improve aerodynamic performance, such as incurved Savonius rotors[26], helical blades[27,28], slotted blades[29], and modifications to the inner blade surface[30]. Additional strategies include the use of external aerodynamic appendages[31], as well as deflector plates positioned upstream[32] and downstream[33] of the rotor. Newly developed Savonius turbine concepts have also been proposed and investigated[34,35].

The noise characteristics of small-scale wind turbines have been investigated through various experimental studies. For example, the power spectral density of acoustic emissions from vertical axis wind turbines in urban environments was analysed under varying wind speeds using wind tunnel experiments[36]. Narrowband and broadband aerodynamic noise components have been investigated numerically[12], experimentally[37], and through field measurements[38]. These studies primarily focused on Darrieus-type turbines. In contrast, noise investigations specific to Savonius wind turbines are limited and primary based on numerical simulations[39,40].

Despite their lower efficiency, Savonius rotors offer several advantages that continue to make them appealing in the market[41]. Firstly, they are well-suited for the wind power requirements of the prosumers, as they can effectively operate with small diameters. Secondly, they boast simplified control systems, as their maintenance is straightforward, often eliminating the need for complex braking systems. Additionally, Savonius rotors possess a unique feature that prevents them from overspinning. This characteristic arises from their behavior in the tip-speed-ratio (TSR) range exceeding 1.2, where they exhibit a tendency to reduce power production as TSR increases, with power disappearing at TSR values greater than approximately 1.8. This inherent simplicity, enhanced by the fact that increasing rotational speed correlates with a reduction in power production, ultimately results in a complete loss of power beyond a certain rotational speed. It's worth noting that reducing the rotor's diameter results in higher rotational speeds. This aspect necessitates careful consideration, particularly for the safety of wind turbines installed near buildings and populated areas.

The proposed Savonius turbine is conceived to ensure effective operation in all wind conditions, achieving high but controlled rotational speeds while avoiding the necessity of shutdown. This ability to operate without interruption, also in challenging weather conditions, offers the added benefit of continuous energy generation when other turbines are forced to cease operations. To achieve these objectives, the rotor has been designed to withstand high centrifugal forces while ensuring safety, particularly in urban environments. Conducting wind tunnel tests on a segment of this prototype wind turbine prior to on-site installation is essential to validate its performance and ensure design reliability.

The tests conducted at the Giovanni Solari Wind Tunnel serve several key purposes: validating the reliability of small wind turbines with small rotor diameters operating at high rotational speeds; assessing performance in smooth and turbulent flow conditions across various operating scenarios; acquiring comprehensive measurements, including undisturbed wind speed, upstream and downstream flow velocities, generated power, rotor rotational speed, and noise emissions. The database of measurements recorded during the experiments is presented with detailed information on methodology and instrumentation. It has been carefully quality-checked and published online[42] to facilitate reuse by the research community and to advance understanding of the Savonius rotor behavior across a wide range of real-world conditions. By examining the performance of the rotor in diverse scenarios, researchers can glean insights into its operational characteristics, efficiency, and limitations. This comprehensive dataset offers valuable opportunities for further analysis, optimization, and refinement of the rotor design, ultimately facilitating the development of more efficient and reliable wind energy technologies.

Methods

Facility and wind tunnel set-up. The experimental tests were carried out at the Giovanni Solari Wind Tunnel of the University of Genoa. It is a closed-circuit type operating at atmospheric pressure with a working section 8.8 m long and a cross-section of 1.70 m (width) × 1.35 m (height). The investigated Savonius rotor features a dual-bucket design, with endplates and five transverse stiffeners to enhance structural integrity. Each bucket consists of two semicylindrical halves, with radius (r) of 65.75 mm, a thickness (t) of 2 mm, and a blade separation gap (g) of 20 mm; the gap ratio ($\gamma = g/2r$) is 0.152. The rotor operates without a central shaft. Crafted from 2 mm thick painted steel sheet and reinforced by welded joints, the entire assembly stands at a height (H) of 1.0 m and a diameter $\Phi = 243$ mm; the aspect ratio (H/Φ) is about 4. Refer to Fig. 1(a,b,c) for a visual depiction of the model configuration.

The model integrates a 3-phase permanent magnet generator (inner rotor type), a torque meter, a Hall sensor, and an AC/DC converter, all connected to a National Instruments NI PXI measurement device. The generator is characterized by a nominal voltage of 48 V and a maximum of 190 V, with nominal and maximum currents of 2 A and 8 A, respectively. Its nominal power output is 300 W, with a maximum output of 750 W. A NCTE 2200-5-A4 torque meter was employed, featuring a measuring range of −5 to 5 Nm and an accuracy of $\leq \pm 1\%$. It provides an analog output signal of 0–5 V and can operate at rotational speeds up to 5000 rpm. To measure mechanical power alongside torque, the Hall sensor incorporates four magnets mounted on a claw coupling within the top support. This arrangement ensures accurate readings in a space shielded from airflow disturbances, with an error of ±1% or less. A manual resistive load is also connected to the generator. The

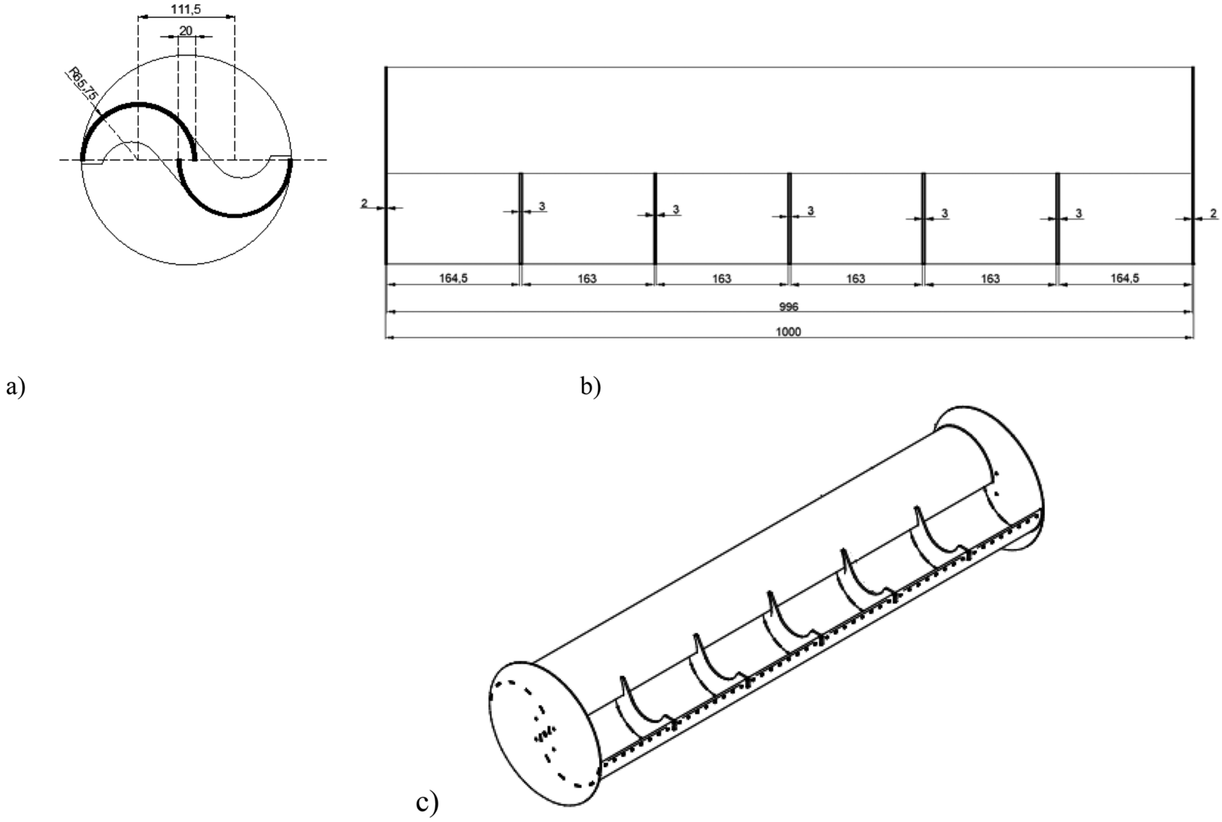

Fig. 1 Blade geometry of the proposed Savonius rotor: plan (**a**), lateral (**b**) and 3D (**c**) views.

output signals from the load and the Hall sensor are converted into a format compatible with the NI system (±10 V DC signal). This setup yields four channels connected to the NI device. One channel is dedicated to torque measurement, feeding directly into the reading system with a signal range of ±5 V. The remaining three channels come from the converter and include current, voltage (±10 V) and Hall sensor data (0 or 5 V). The power converter necessitates a 12 V DC power supply, which is facilitated through a 230 V AC power source.

The rotor model, with the generator and associated electronics, has been positioned vertically within the wind tunnel (Fig. 2), securely anchored to both the floor and the ceiling to ensure a stable and robust mounting. Precautions to safeguard the tunnel infrastructure included the installation of wooden panels along the walls and floor, as well as the fitting of a protective net at the tunnel outlet.

Two different passive grids[43], with different mesh and bar sizes, have been used for generating atmospheric turbulence. With reference to Fig. 3a, the thick grid (Fig. 3b) has dimensions $M = 155$ mm, $B = 40$ mm, $D = 15$ mm, while the thin grid (Fig. 3c) has $M = 155$ mm, $B = 15$ mm, $D = 15$ mm. They were placed at 2.0 m upstream the turbine.

A Pitot-static tube records wind velocity at the wind tunnel inlet at 2 kHz, positioned 2.4 m upstream of the turbine and 40 cm upstream of the grid. Additionally, a TFI Cobra Probe has been used for measuring the undisturbed flow field at the turbine position in the empty wind tunnel. The accuracy of the sensor is ± 0.5 m/s.

Moreover, two hot wire anemometers (Dantec 55P11) are utilized, connected with a Mini CTA 54T30 type also recording at 2 kHz. These instruments measure flow velocities at a distance of one rotor diameter Φ upstream (hot wire 2) and 3-Φ downstream of the rotor (hot wire 1), at a height of 0.56 m above the wind tunnel floor (Fig. 4a). Ambient temperature is also recorded. Four omni-directional, prepolarized free-field microphone 1/2", Bruel&Kjaer type 4189 A-021 (inherent noise is 16.5 dB A, lower limiting frequency is 12 Hz at -3dB), are positioned at the wind tunnel ceiling for noise measurements. The first microphone is placed at a distance Φ from the outer edge of the rotor, while the others are positioned at distances of 1 m, 2 m, and 4 m (Fig. 4b).

Figure 5 provides a schematic overview of the instrumentation layout and the wind tunnel set-up, illustrating the relative positions of the grid, probes, microphones and turbine model within the test chamber.

Preliminary tests. Preliminary tests were conducted in the empty wind tunnel to characterize the flow, as well as on the wind turbine rotating at different speeds. The undisturbed wind flow was characterized using a Cobra probe placed at the model's position in the absence of the model, since the Pitot tube at the tunnel inlet could be influenced by local disturbances from the turbulence-generating grid. These measurements provided the undisturbed wind velocity v at the turbine position (which is assumed as the free stream velocity) and the

Fig. 2 Model in the wind tunnel.

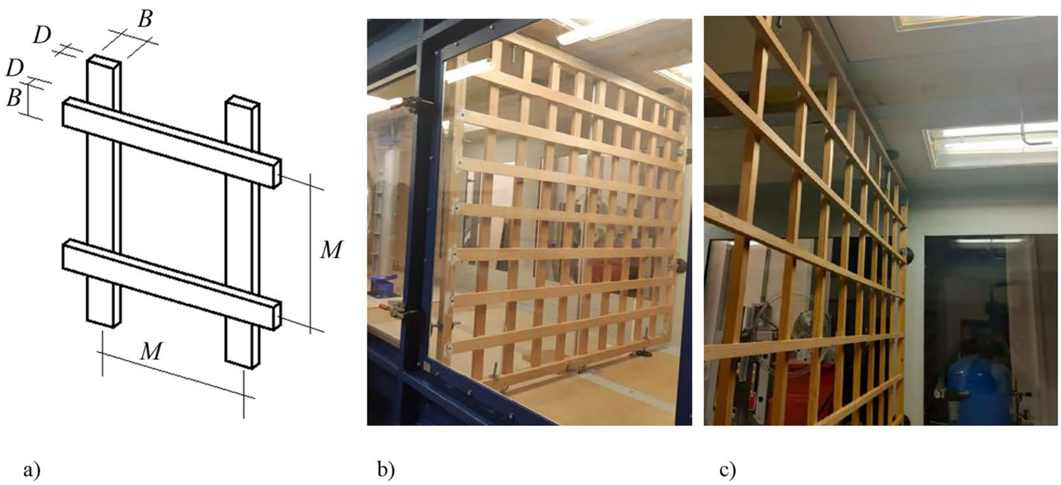

Fig. 3 Passive grid: schematic (**a**), thick grid (**b**) and thin grid (**c**) positioned in the wind tunnel.

longitudinal turbulence intensity I_u. Table 1 presents the values of v and I_u for different rotational frequency f of the wind tunnel fan obtained under smooth flow conditions (referred to as *T0*) and with passive grids used to generate turbulent flow. Condition *T4* was generated using the thin grid, resulting in an average $I_u = 4\%$; condition *T8* was created using the thick grid, yielding an average $I_u = 8\%$. The relationship between the fan frequency and the undisturbed flow velocity under the different conditions *T0*, *T4*, and *T8* is well approximated by the following linear laws:

$$\begin{aligned} v &= 0.53\ f \quad \text{condition } T0 \\ v &= 0.50\ f \quad \text{condition } T4 \\ v &= 0.38\ f \quad \text{condition } T8 \end{aligned} \tag{1}$$

For the flow measurements, the hot-wire probes were calibrated using King's law. The calibration was performed in the empty wind tunnel under steady inflow conditions, over a wind velocity range of 4–21 m/s, measured at the inlet by a Pitot tube using 8 discrete calibration points. The ambient temperature was monitored and remained stable at 28.1 °C. Similar environmental conditions were maintained during the subsequent measurements, thereby minimizing thermal drift effects.

The calibration coefficients were obtained through a least-squares fit of King's law to the measured voltage, V_{hw} - velocity data, v_p. The empirical relationship between V_{hw}, and v_p is described by:

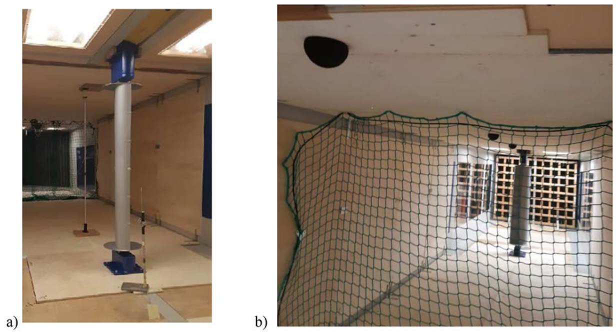

Fig. 4 Hot wires (**a**) and microphones (**b**) placed in the wind tunnel.

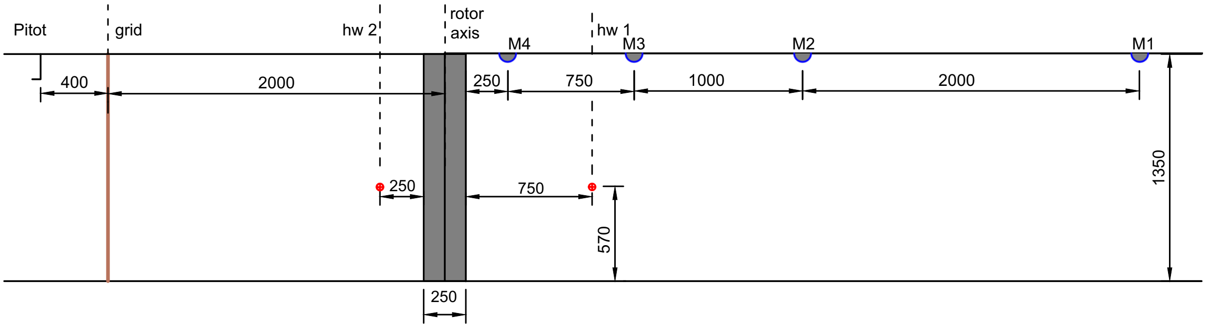

Fig. 5 General schematic of the wind tunnel set up, with airflow direction from left to right.

	no grid	*T0*	thin grid	*T4*	thick grid	*T8*
f	*v*	I_u	*v*	I_u	*v*	I_u
(Hz)	(m/s)	(%)	(m/s)	(%)	(m/s)	(%)
8	4.1	1.0	3.8	4.2	2.8	8.4
12	6.3	0.4	5.9	3.9	4.4	8.1
16	8.4	0.4	7.9	3.9	6.0	7.6
20	10.5	0.3	10.0	3.8	7.6	7.8
24	12.8	0.2	11.9	3.9	9.3	7.5
28	15.0	0.2	14.0	3.9	10.8	7.0
32	17.0	0.2	16.1	3.6	12.4	7.5

Table 1. Overview of flow conditions.

$$V_{hw}^2 = \mathrm{A} + \mathrm{B}v_p^n \tag{2}$$

where n is set to 0.45[44], and the coefficients A and B are obtained by fitting the V_{hw} and V_p data via least-squares regression, with $R^2 > 0.999$ (coefficient of determination).

Additional preliminary tests were then carried out to explore the overall experimental setup, including checking the measurement system, assessing high-frequency torque measurements, exploring rotor performance at high wind speeds, and determining the maximum wind speed for safe operation. These exploratory tests are not reported and discussed in detail here.

Main test campaign. The main test campaign was conducted in three stages. The first phase (Stage I, July 2023) was primarily exploratory, and was carried out at various wind tunnel fan frequencies in order to obtain a general understanding of the turbine's behavior under smooth inflow conditions.

The second phase (Stage II, July 31 – August 8, 2023) was specifically aimed at investigating the power and torque, as well as the wind flow upstream and downstream of the rotor, under both smooth and turbulent inflow conditions. Tests under smooth flow were conducted for wind tunnel fan frequencies ranging from $f = 8$ Hz to 40 Hz, with a step size of 4 Hz. Tests under turbulent flow were conducted in the range $f = 6$ Hz to 16 Hz with a step size of 2 Hz, for condition *T4* and in the range $f = 4$ Hz to 14 Hz with a step size of 2 Hz, for condition *T8*. Hot wire calibrations were performed at the beginning of this phase (July 31).

These tests were repeated in third and final phase (Stage III, September 2023) which was specifically dedicated to acoustic noise measurements. Additional frequencies were also investigated during this phase.

Tests were performed following the procedure outlined below. For each wind tunnel fan frequency (*i.e.*, wind speed), the wind tunnel was first brought to steady-state, as verified by the Pitot probe measurement at the inlet. The turbine was initially operated under a low load. Once steady rotational conditions were achieved, a 60-second acquisition of all relevant quantities was recorded. The load was then progressively increased in discrete steps, allowing the rotor to reach a new steady state before recording the next 60 s measurement. This incremental procedure was continued until the turbine approached near standstill conditions. The load step size was not fixed a priori but was adjusted manually by the operator during the test in order to achieve a sufficiently dense sampling of the power curve. In particular, smaller load increments were applied in the region close to the maximum power point, while larger increments were used in regions characterized by a smoother power variation.

The following time histories were acquired:

- wind velocity v_p (m/s) at the test section inlet, measured using a Pitot static tube;
- wind tunnel temperature t (°C), measured with a thermometer;
- electric generator output, voltage V (V) and current i (A);
- Hall sensor voltage signals (V), used to detect rotor angular position;
- torque at the rotor axis T (Nm), measured with a torquemeter;
- wind velocity v_{hw} (m/s) upstream (1-Φ) and downstream (3-Φ) of the turbine's outer edge, measured using CTAs;
- acoustic noise pressure p (Pa) at four positions downstream of the turbine, measured with microphones.

The sampling rate is 2000 Hz, except for the acoustic measurements, which are acquired at 65,536 Hz.

The rotor speed was obtained from the frequency of the dominant peak in the power spectrum of the Hall sensor signal. Since the sensor generated four pulses per revolution (four magnets on the rotor), the measured frequency was divided by 4 and multiplied by 60 to obtain the rotational speed ω in rpm. The mechanical power P (W) was derived from rotational speed and torque:

$$P = \frac{2\pi\omega}{60}T \tag{3}$$

The maximum rotor rotational speed achieved was nearly 2500 rpm at $f = 40$ Hz in smooth flow.

Noise measurements. During Stage III, noise measurements were performed in the wind tunnel with forced airflow at various velocities. These conditions produced heterogeneous sound propagation and background noise levels. To avoid disturbances caused by airflow and direct wind pressure on the microphone diaphragm, the microphones were positioned to minimize flow interference. Since the volume velocity in a duct decreases toward its walls[45], the optimal mounting location was identified as the ceiling of the duct. Moreover, the microphones were equipped with 90 mm diameter windscreens to further reduce flow-induced noise. The nonlinear spatial arrangement of the microphones (Fig. 5) relative to the rotor reflects the nonlinear decay of the sound pressure level (SPL) in the free field, as for each doubling of distance, the SPL decreases by approximately 6 dB[45].

To minimize uncertainty due to microphone variability, calibration was performed before and after the measurement campaign using an external reference source (Brüel & Kjær Type 4231 sound calibrator).

Preliminary measurements were performed to assess background noise under three different static conditions in smooth flow: '*T0 empty*', i.e., with the wind tunnel completely empty, '*T0 no rotor*', with only the rotor mounting system installed but without the rotor, and '*T0 still*', with the rotor installed but held fixed in its minimum-drag position, without rotation.

Main measurements have been conducted in smooth and turbulent flow by varying the load at each selected wind tunnel velocity, using the same procedure already illustrated in the previous section. Tests in smooth flow are referred to as '*T0* rotating' and explored the wind tunnel fan frequencies from 8 Hz to 32 Hz in steps of 4 Hz. Tests in turbulent flow are referred to as '*T4* rotating' and '*T8* rotating', corresponding to conditions *T4* and *T8*, respectively, and were carried out by choosing f to reproduce the same speed v that was recorded in condition *T0*. Table 2 reports the test schedule.

Data Records

The dataset is available at Zenodo[42]. It includes a schematic summary of the data resumed in three Excel files, named 'STAGE I.xlsx', 'STAGE II.xlsx', 'STAGE III.xlsx', each listing the average results of the runs conducted during the corresponding test stage. The first column, labeled 'Date', reports the timestamp of the experiment in the format *yyyymmdd_hhmmss*. The subsequent columns contain the mean values of the following quantities:

- Speed, v_p (m/s) – flow velocity measured by the Pitot at the wind tunnel inlet;
- Inverter, f (Hz) –frequency of the wind tunnel propeller;
- Temperature, t (°C) – air temperature inside the wind tunnel;
- Volts, V (V) – generated voltage;
- Current, i (A) – generated current;
- RPM, ω (rpm) – turbine rotational speed per minute
- Torque, T (Nm) – torque generated by the turbine;
- Hotwire1, (m/s) – flow velocity recorded by the 3-Φ downstream hotwire

wind tunnel set-up	*f* (Hz)						
T0 empty	8	12	16	20	24	28	32
T0 no rotor	8	12	16	20	24	28	32
T0 still rotor	8	12	16	20	24	28	32
T0 rotating	8	12	16	20	24	28	32
T4 still rotor	—	12.7	16.9	21.1	25.2	29.6	—
T4 rotating	—	12.7	16.9	21.1	25.2	29.6	—
T8 still rotor	—	15.4	21.0	26.7	32.4	38.1	—
T8 rotating	—	15.4	21.0	26.7	32.4	38.1	—
v (m/s)	4.1	6.3	8.4	10.5	12.8	15.0	17.0

Table 2. List of noise measurement tests.

Date	Speed (m/s)	Inverter (Hz)	Temperature (°C)	Volts (V)	Current (a)	RPM (rpm)	Torque (Nm)	Hotwire1 (m/s)	Hotwire2 (m/s)	Type Grid
'20230808_140525'	3.89	10.5	28.88	20.27	0.00	266	−0.0660	2.06	4.06	8
'20230808_140845'	3.89	10.5	28.83	17.02	0.02	230	−0.0739	2.02	4.07	8
'20230808_141133'	3.89	10.5	28.79	13.81	0.03	194	−0.0824	2.10	4.07	8
'20230808_141432'	3.88	10.5	28.75	12.04	0.04	174	−0.0871	2.14	4.08	8
'20230808_141744'	3.89	10.5	28.70	8.92	0.06	137	−0.0943	2.03	4.08	8
'20230808_142320'	3.89	10.5	28.62	0.54	0.06	29	−0.0872	2.39	4.08	8
'20230808_142822'	5.97	15.7	28.68	42.97	0.00	545	−0.0872	3.81	5.69	8
'20230808_143118'	5.97	15.7	28.67	40.05	0.03	513	−0.1040	3.56	5.70	8
'20230808_143456'	5.97	15.7	28.66	39.75	0.03	512	−0.1056	3.55	5.66	8
'20230808_143941'	5.97	15.7	28.65	37.22	0.05	484	−0.1197	3.37	5.72	8
..	….	….	….	….	….	….	…..	….	….	…

Table 3. Data overview example from Excel files.

- Hotwire2, (m/s) – flow velocity recorded by the 1-*Φ* upstream hotwire

Last column, Type Grid, specifies the flow condition: 0, 4, 8 corresponding to conditions *T0*, *T4*, *T8*, respectively.

In Table 3 an excerpt from one of these files is presented for reference. A negative sign in *T* indicates that the rotor is driving.

For each test entry (identified by *Date* = *yyyymmdd_yymmss*), the correspondent time histories of the recorded quantities are listed in the Matlab file: *Date*.mat. In this case, the variable labeled RPM reports the Hall sensor voltage signal. The files are stored in 3 zip archives, namely, 'STAGE I.zip', 'STAGE III.zip', 'STAGE III.zip'.

Noise measurements from the four microphones M1-M4 are provided in a series of files labeled *Label1*'F'*Label2*'P'*Label3*'-1.wav' according to the different scenarios (the characters in quotation marks are fixed identifiers and the labels encode specific test conditions). *Label1* indicates the test conditions:

- 'empty tunnel' – under smooth flow, with rotor and all mounting elements removed;
- 'NoRotor' – under smooth flow, with rotor removed and only the mounting elements (handles) inside the wind tunnel;
- 'Tlo' – under smooth flow, with rotor installed but not rotating;
- 'T0' – turbine rotating in smooth flow (condition *T0*);
- 'T4' – turbine rotating in turbulent flow (condition *T4*);
- 'T8' – turbine rotating in turbulent flow (condition *T8*).

Label2 = XX, being XX = 08, 12, 16…, represents the fan frequency of the wind tunnel that, in smooth flow, supplies the value of v_p recorded in the test. In condition *T0*, it coincides with the frequency of the wind tunnel propeller. In condition *T4* and *T8* it can be read in Table 2. To give an example, in condition *T4*, *Label2* = 12 corresponds to *f* = 12.7 Hz.

Label3 is the order number of the steady-state recording, corresponding to subsequent steps of the load, being step 1 the highest load. In the case where *Label1* corresponds to 'empty tunnel' or 'NoRotor', or 'Tlo', then *Label3* = 1, as there is no load on the wind turbine.

These noise measurement tests correspond to rows of the 'stage_III.xlsx' file with the following date labels: rotor stopped (*Label1* = 'Tlo'), from '20230928_095229' to '20230928_100156'; rotating turbine in smooth flow *T0* (*Label1* = 'T0', *Label2* = 08, 12, …), from '20230928_100911' to '20230928_130207'; rotating turbine in turbulent flow *T4* (*Label1* = T4, *Label2* = 12, 16 …), from '20230927_152547' to '20230928_093941'; rotating turbine in turbulent flow *T8* (*Label1* = T8, *Label2* = 12, 16 …), from '20230927_093855' to '20230927_111858';

rotor removed (*Label1* = 'NoRotor'), from '20230928_145859' to '20230928_150648'; empty tunnel (*Label1* = 'EmptyTunel'), from '20230928_152643' to '20230928_153429'.

Each .wav file contains the 60-second recording of the four microphones. The files are stored in six ZIP archives, each with a filename starting with the prefix 'wav'.

Technical Validation

Measurements are affected by uncertainties that may arise primarily from scaling effects, bearing friction, and instrument accuracy. Generally, scaling-related uncertainties cannot be fully controlled or accurately assessed[46]. However, in the present experiment, the model closely represents a real-scale micro wind turbine, thereby eliminating issues associated with geometric and dynamic similarity. Moreover, the careful design and validation of the test setup ensure that bearing friction can be regarded as negligible.

The wind speed v, the rotational velocity ω and the torque T are the primary measured variables for the wind turbine performance assessment. The reference wind speed was determined as the average of five measurements acquired using the Cobra probe at different points in the test section and was further validated by means of a Pitot static tube and a hot-wire anemometer. The overall error in the wind speed is estimated to be ± 0.15 m/s, accounting for possible variations among the measurement devices and environmental conditions. The accuracy of the torque and rotation measurements is $\pm 1\%$.

Turbulent fluctuations recorded with CTA probe are affected by background noise. In smooth flow, based on previous repeated characterizations, the turbulence intensity in the empty wind tunnel is expected to be below $I_u = 0.2\%$. However, CTA measurements upstream of the turbine under smooth conditions show higher turbulence values, reaching up to $I_u = 0.8$–1%. This suggests that turbulence measurements taken upstream of the wind turbine in smooth flow should be considered only indicative and may not accurately represent the true turbulence characteristics of the facility.

For the sound measurements, the primary source of uncertainty is determined by the microphone specifications, particularly their inherent noise of 16.5 dB A.

To technically validate the experiments, both the repeatability of the measurements and their agreement with available literature data are assessed.

Repeatability cannot be directly assessed, as the applied load steps generally vary between tests, even under the same flow conditions. Therefore, the analysis is conducted in terms of the power coefficient (c_p) and torque coefficient (c_T) curves versus the tip speed ratio (TSR). They are defined by:

$$c_p = \frac{P}{\frac{1}{2}\rho v^3 A_s}; \quad c_T = \frac{T}{\frac{1}{2}\rho v^2 R A_s}; \quad \mathrm{TSR} = \frac{2\pi}{60}\frac{\omega R}{v} \tag{4}$$

where ρ (kg/m^3) is the air density, A_s (m^2) is the turbine swept area, $R = \Phi/2$ (m) is the turbine external radius, v (m/s) is the free stream wind velocity. Through Eqs. (3) and (4), uncertainties associated with the measurement of v, ω, T propagate to the derived quantities c_p, c_T, and TSR[47].

By expanding c_p, c_T, and TSR in Taylor series and applying the statistical operators, their statistical moments can be obtained from the product of the partial derivatives of c_p, c_T, and TSR with respect to v, ω, T and the statistical moments of v, ω, T[48,49]. By analytically developing these partial derivatives, one obtains:

$$\begin{aligned}
\sigma_{c_p} &= c_p\sqrt{\left(\frac{\sigma_\omega}{\omega}\right)^2 + \left(\frac{\sigma_T}{T}\right)^2 + \left(3\frac{\sigma_v}{v}\right)^2} \\
\sigma_{c_T} &= c_T\sqrt{\left(\frac{\sigma_\omega}{\omega}\right)^2 + \left(\frac{\sigma_T}{T}\right)^2 + \left(2\frac{\sigma_v}{v}\right)^2} \\
\sigma_{TSR} &= TSR\sqrt{\left(\frac{\sigma_\omega}{\omega}\right)^2 + \left(\frac{\sigma_v}{v}\right)^2}
\end{aligned} \tag{5}$$

where $\sigma_{[\bullet]}$ denotes the standard deviation of $[\bullet]$. In Eq. (5), v, ω and T represent the nominal measured values, while c_p, c_T, and TSR denote the values computed from Eq. (4) using those nominal values.

Assuming a uniform distribution of the errors in v, ω and T within the instrument precision range, the corresponding standard deviations σ_v, σ_ω, σ_T are evaluated by dividing the maximum error by $\sqrt{3}$.

Figure 6 shows the power and torque coefficients versus the TSR with their associated uncertainties at wind speeds 4.2 m/s and 12.7 m/s. Discrepancies observed among repeated measurements are consistently lower than this standard uncertainty.

Along this line, repeatability can be checked and verified across all multiple tests conducted between July and September 2023 where, at the end of each test stage, the turbine and the experimental setup were dismantled and re-assembled in the successive stage.

The comparison with experiments reported in the literature raises the issue of ensuring homogeneous conditions. Experimental studies on Savonius turbines show considerable variability, largely due to differences in design parameters such as aspect ratio, gap ratio, blade profile, number of blades, rotor radius, number of stages, end plates, and bearing type[50–53]. This diversity makes direct comparisons challenging and complicates the identification of consistent performance trends.

A meaningful comparison can be drawn with the experiments by Blackwell *et al.*[54], who conducted an extensive test campaign on Savonius turbines, systematically varying the number of buckets, gap spacing, aspect ratio, and wind speed. From the configurations tested, we selected the one closest to our setup: two semicircular

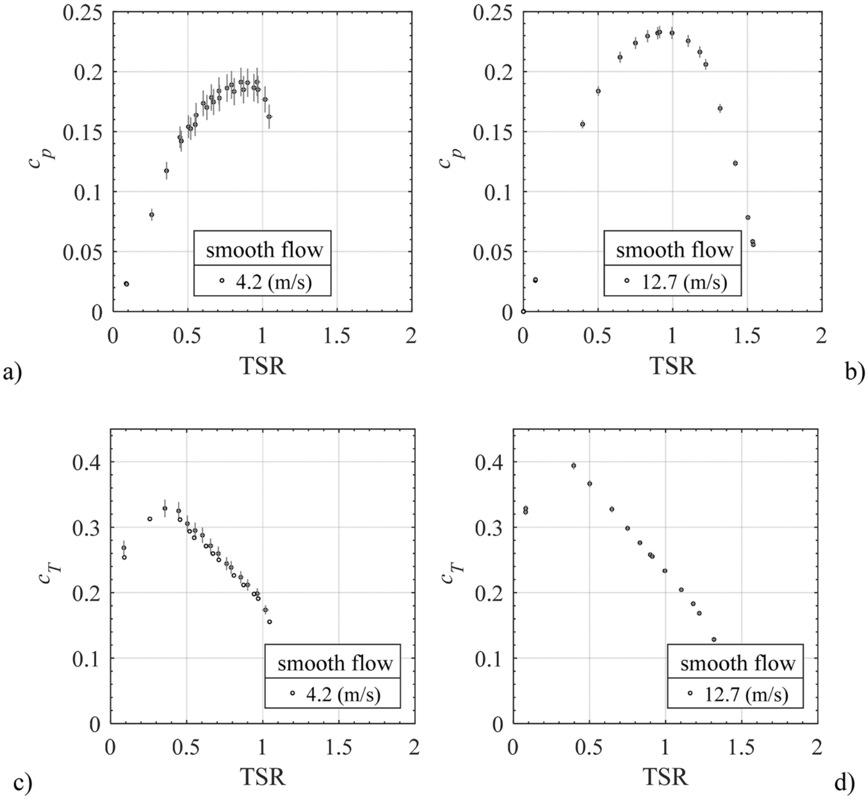

Fig. 6 Power coefficient curves (**a,b**) and torque coefficient curves (**c,d**) at 4.2 m/s and 12.7 m/s from repeated tests and associated uncertainty intervals.

aluminum buckets, $\Phi = 0.5$ m, $H/\Phi = 2$, $\gamma = 0.15$, tested at a free-stream velocity of 14 m/s, under a turbulence intensity $I_u = 1.4\%$. The corresponding Reynolds number was $Re = 4.3 \times 10^5$.

To enhance any comparison, the data should be corrected for blockage effects. The velocity increment is influenced by both wake and solid blockage, making its estimation a delicate issue due to the complexity of the aerodynamic phenomena involved[55,56]. In this study, these effects are accounted for using the following correction factor, proposed for unusual shapes tested in wind tunnels[57]:

$$\varepsilon_t = \frac{1}{4}\frac{\text{model frontal area}}{\text{test section area}} \tag{6}$$

where $\varepsilon_t = 0.036$ for the present experiment. The corrected velocity is given by:

$$v_c = v(1 + \varepsilon_t) \tag{7}$$

where v_c is the free-stream corrected velocity and v is the uncorrected value. It should be noted that the use of this coefficient introduces an additional source of uncertainty in the estimated power and torque, which can be quantified by considering a variability of ε_t equal to $\pm 0.5\varepsilon_t$[54]. However, the resulting uncertainty remains small compared with that associated with the velocity measurement.

In Fig. 7, selected results from Blackwell's experiments are compared with those obtained in the present study under smooth flow conditions at $f = 40$ Hz, $v = 21.9$ m/s and $Re = 3.5 \times 10^5$, selected to closely match the Blackwell tests. The c_T curves shows some discrepancies at lower TSR, while the c_p curves are quite well aligned.

A further validation concerns the estimation of the turbine's rotational speed. Since the Hall sensor produces a discrete output signal, directly determining the rotational velocity is not straightforward. To address this, the frequency corresponding to the highest peak in the power spectrum of the sensor output is identified. For example, Fig. 8 shows the PSD of the Hall sensor signal during one of the experiments, highlighting this peak frequency. The rotational speed is then calculated following the procedure described in the Methods section. This approach is further supported by the consistency of these frequencies with those that one could observe in hot-wire measurements and in noise spectra.

Data availability

The experimental data collected during the wind tunnel tests are publicly available in the Zenodo repository at https://doi.org/10.5281/zenodo.18892811.

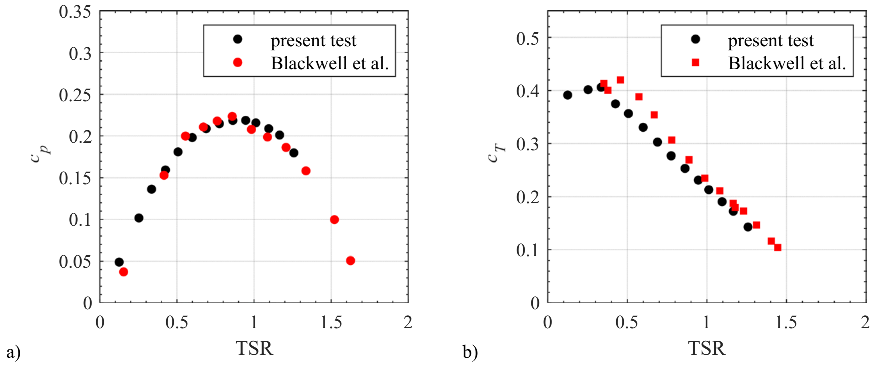

Fig. 7 Power (**a**) and torque coefficient (**b**) from the present study (smooth flow, $f = 40$ Hz) compared with data from Blackwell *et al.*[54] at similar Reynolds number.

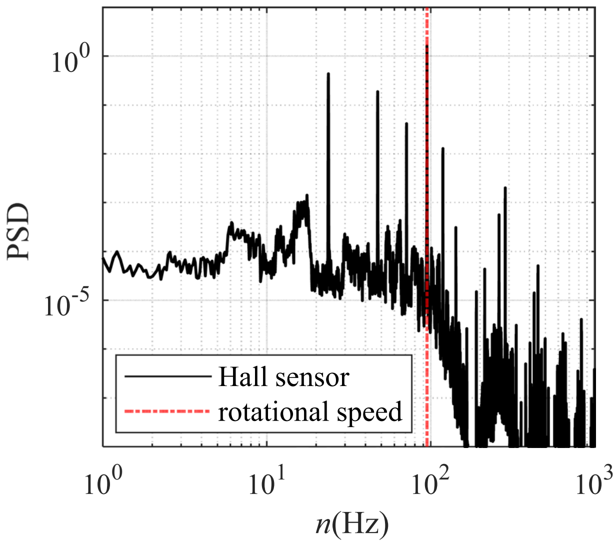

Fig. 8 Example of PSD from Hall sensor measurements used to determine the turbine rotational frequency.

Code availability

The datasets are provided as .mat files (time histories of raw measurements excluding acoustic pressure), .xlsx files (averaged values), and .wav files (time histories of acoustic pressure). The MATLAB script 'read_RPM_Z.m', available in the same Zenodo repository, reproduces the calculation of the rotor's average rotational speed (rpm) from the Hall sensor signal.

Received: 1 August 2025; Accepted: 30 March 2026;
Published online: 06 April 2026

References

1. Stathopoulos, T., Alrawashdeh, H., Al-Quraan, …, Paraschivoiu, M. & Pilay, P. Urban wind energy: Some views on potential and challenges. *Journal of Wind Engineering and Industrial Aerodynamics* **179**, 146–157, https://doi.org/10.1016/j.jweia.2018.05.018 (2018).
2. de Simon-Martín, M., Ciria-Garcés, T., Rosales-Asensio, E. & Gonzalez-Martínez, A. Multi-dimensional barrier identification for wind farm repowering in Spain through an expert judgment approach. *Renewable and Sustainable Energy Reviews* **161**, 112387, https://doi.org/10.1016/j.rser.2022.112387 (2022).
3. Irie, N. & Kawahara, N. Consumer preferences for local renewable electricity production in Japan: A choice experiment. *Renewable Energy* **182**, 1171–1181, https://doi.org/10.1016/j.renene.2021.10.028 (2022).
4. Pagnini, L. C., Burlando, M. & Repetto, M. P. Experimental power curve of small-size wind turbines in turbulent urban environment. *Applied Energy* **154**, 112–21, https://doi.org/10.1016/j.apenergy.2015.04.117 (2015).
5. Pagnini, L., Piccardo, G. & Repetto, M. P. Full scale behavior of a small size vertical axis wind turbine. *Renewable Energy* **127**, 41–55, https://doi.org/10.1016/j.renene.2018.04.032 (2018).
6. Pagnini, L., Bracco, S., Delfino, F. & de-Simón-Martín, M. Levelized cost of electricity in renewable energy communities: Uncertainty propagation analysis. *Applied Energy* **366**, 123278, https://doi.org/10.1016/j.apenergy.2024.123278 (2024).
7. Anderson, B., Rane, J. & Khan, R. Distributed wind-hybrid microgrids with autonomous controls and forecasting. *Applied Energy* **333**, 120557, https://doi.org/10.1016/j.apenergy.2022.120557 (2023).
8. Wilberforce, T., Olabi, A. G., Sayed, E. T., Alalmi, A. H. & Abdelkareem, M. A. Wind turbine concepts for domestic wind power generation at low wind quality sites. *Journal of Cleaner Production* **394**, 136137, https://doi.org/10.1016/j.jclepro.2023.136137 (2023).

9. Orrell, A., Sheridan, L., Kazimierczuk, K. & Fensch, A. Distributed Wind Market Report: 2023 Edition (Pacific Northwest National Laboratory, 2023).
10. Ani, S. O., Polinder, H. & Ferreira, J. A. Comparison of energy yield of small wind turbines in low wind speed areas. *IEEE Transactions on Sustainable Energy* **4**(1), 42–49, https://doi.org/10.1109/TSTE.2012.2197426 (2013). 6216474.
11. Pagnini, L. & Piccardo, G. Modal properties of a vertical axis wind turbine in operating and parked conditions. *Engineering Structures* **242**, 112587, https://doi.org/10.1016/j.engstruct.2021.112587 (2021).
12. Mohamed, M. H. Aero-acoustics noise evaluation of H-rotor Darrieus wind turbines. *Energy* **65**, 596–604, https://doi.org/10.1016/j.energy.2013.11.031 (2014).
13. Pedersen, E. & Persson Waye, K. Perception and annoyance due to wind turbine noise—a dose–response relationship. *The Journal of the Acoustical Society of America* **116**, 3460–3470, https://doi.org/10.1121/1.1815091 (2004).
14. Abohela, I., Hamza, N. & Dudek, S. Effect of roof shape, wind direction, building height and urban configuration on the energy yield and positioning of roof mounted wind turbines. *Renewable Energy* **50**, 1106–1118, https://doi.org/10.1016/j.renene.2012.08.068 (2013).
15. Juan, Y.-H., Wen, C.-Y., Li, Z. & Yang, A.-S. Impacts of urban morphology on improving urban wind energy potential for generic high-rise building arrays. *Applied Energy* **299**, 117304, https://doi.org/10.1016/j.apenergy.2021.117304 (2021).
16. Tan, X. *et al*. A self-adapting wind energy harvesting system for application in canyon bridge. *Sustainable Energy Technologies and Assessments* **54**, 102878, https://doi.org/10.1016/j.seta.2022.102878 (2022).
17. Kumar, R., Raahemifar, K. & Fung, A. S. A critical review of vertical axis wind turbines for urban applications. *Renewable and Sustainable Energy Reviews* **89**, 281–291, https://doi.org/10.1016/j.rser.2018.03.033 (2018).
18. Orlando, A., Pagnini, L. & Repetto, M. P. Structural response and fatigue assessment of a small vertical axis wind turbine under stationary and non-stationary excitation. *Renewable Energy* **170**, 251–266, https://doi.org/10.1016/j.renene.2021.01.123 (2021).
19. Akwa, J. V., Vielmo, H. A. & Petry, A. P. A review on the performance of Savonius wind turbines. *Renewable and Sustainable Energy Reviews* **16**(5), 3054–3064, https://doi.org/10.1016/j.rser.2012.02.056 (2012).
20. Dewan, A., Gautam, A. & Goyal, R. Savonius wind turbines: A review of recent advances in design and performance enhancements. *Materials Today: Proceedings* **47**(11), 2976–2983, https://doi.org/10.1016/j.matpr.2021.05.205 (2021).
21. Modi, V. J. & Fernando, M. S. U. K. On the performance of the savonius wind turbine. *Journal of Solar Energy Engineering Transactions of the ASME* **111**(1), 71–81 (1989).
22. Hayashi, T., Li, Y. & Hara, Y. Wind tunnel tests on a different phase three-stage Savonius rotor. *JSME International Journal Series B Fluids and Thermal Engineering* **48**, 9–16, https://doi.org/10.1299/jsmeb.48.9 (2005).
23. Saha, U. K., Thotla, S. & Maity, D. Optimum design configuration of Savonius rotor through wind tunnel experiments. *Journal of Wind Engineering and Industrial Aerodynamics* **96**(8-9), 1359–1375, https://doi.org/10.1016/j.jweia.2008.03.005 (2008).
24. Mahmoud, N. H., El-Haroun, A. A., Wahba, E. & Nasef, M. H. An experimental study on improvement of Savonius rotor performance. *Alexandria Engineering Journal* **51**(1), 19–25, https://doi.org/10.1016/j.aej.2012.07.003 (2012).
25. Wenehenubun, F., Saputra, A. & Sutanto, H. An experimental study on the performance of Savonius wind turbines related with the number of blades. *Energy Procedia* **68**, 297–304, https://doi.org/10.1016/j.egypro.2015.03.259 (2015).
26. Driss, Z., Mlayeh, O., Driss, D., Maaloul, M. & Abid, M. S. Numerical simulation and experimental validation of the turbulent flow around a small incurved Savonius wind rotor. *Energy* **74**, 506–517, https://doi.org/10.1016/j.energy.2014.07.016 (2014).
27. Kothe, L. B., Möller, S. V. & Petry, A. P. Numerical and experimental study of a helical Savonius wind turbine and a comparison with a two-stage Savonius turbine. *Renewable Energy* **148**, 627–638, https://doi.org/10.1016/j.renene.2019.10.151 (2020).
28. Saad, A. S., Elwardany, A., El-Sharkawy, I. I., Ookawara, S. & Ahmed, M. Performance evaluation of a novel vertical axis wind turbine using twisted blades in multi-stage Savonius rotors. *Energy Conversion and Management* **235**, 114013, https://doi.org/10.1016/j.enconman.2021.114013 (2021).
29. Tjahjana, D. D. D. P. *et al*. Experimental study of the effect of slotted blades on the Savonius wind turbine performance. *Theoretical and Applied Mechanics Letters* **11**(3), 100249, https://doi.org/10.1016/j.taml.2021.100249 (2021).
30. Al-Absi, S. M., Jabbar, A. H., Mezan, S. O., Al-Rawi, A. B. & Al-Alattabi, S. T. An experimental test of the performance enhancement of a Savonius turbine by modifying the inner surface of a blade. *Materials Today: Proceedings* **42**, 2233–2240, https://doi.org/10.1016/j.matpr.2020.12.309 (2021).
31. Montelpare, S., D'Alessandro, V., Zoppi, A. & Ricci, R. Experimental study on a modified Savonius wind rotor for street lighting systems. Analysis of external appendages and elements. *Energy* **144**, 146–158, https://doi.org/10.1016/j.energy.2017.12.017 (2018).
32. Golecha, K., Eldho, T. I. & Prabhu, S. V. Influence of the deflector plate on the performance of modified Savonius water turbine. *Applied Energy* **88**(9), 3207–3217, https://doi.org/10.1016/j.apenergy.2011.03.025 (2011).
33. Guo, F., Song, B., Mao, Z. & Tian, W. Experimental and numerical validation of the influence on Savonius turbine caused by rear deflector. *Energy* **196**, 117132, https://doi.org/10.1016/j.energy.2020.117132 (2020).
34. Roy, S. & Saha, U. K. Wind tunnel experiments of a newly developed two-bladed Savonius-style wind turbine. *Applied Energy* **137**, 117–125, https://doi.org/10.1016/j.apenergy.2014.0.022 (2015).
35. Mercado-Colmenero, J. M., Rubio-Paramio, M. A., Guerrero-Villar, F. & Martin-Doñate, C. A numerical and experimental study of a new Savonius wind rotor adaptation based on product design requirements. *Energy Conversion and Management* **158**, 210–234, https://doi.org/10.1016/j.enconman.2017.12.058 (2018).
36. Li, S. *et al*. Experimental investigation on noise characteristics of small scale vertical axis wind turbines in urban environments. *Renewable Energy* **200**, 970–982, https://doi.org/10.1016/j.renene.2022.09.099 (2022).
37. Pearson, C. E. & Graham, W. R. Experimental characterization of vertical-axis wind turbine noise. *The Journal of the Acoustical Society of America* **137**, EL111, https://doi.org/10.1121/1.4904915 (2015).
38. Ottermo, F., Möllerström, E., Nordborg, A., Hylander, J. & Bernhoff, H. Location of aerodynamic noise sources from a 200 kW vertical-axis wind turbine. *Journal of Sound and Vibration* **400**, 154–166, https://doi.org/10.1016/j.jsv.2017.03.033 (2017).
39. Kim, S. & Cheong, C. Development of low-noise drag-type vertical wind turbines. *Renewable Energy* **79**, 199–208, https://doi.org/10.1016/j.renene.2014.09.047 (2015).
40. Malainine, M., Khaled, A. & Shabaan, S. M. Aeroacoustics behavioral study of Savonius wind turbine. *Journal of Physics: Conference Series* **2128**(1), 012033, https://doi.org/10.1088/1742-6596/2128/1/012033 (2021).
41. Roy, S. & Saha, U. K. Review of experimental investigations into the design, performance and optimization of the Savonius rotor. *Proceedings of the Institution of Mechanical Engineers, Part A: Journal of Power and Energy* **227**(4), 528–542, https://doi.org/10.1177/0957650913480992 (2013).
42. Doerffer, K. *et al*. ERIES - THRUST dataset: The High Rotational Urban Savonius Turbine [Data set]. *Zenodo* https://doi.org/10.5281/zenodo.18892811 (2026).
43. Vita, G., Hemida, H., Andrianne, T. & Baniotopoulos, C. C. Generating atmospheric turbulence using passive grids in an expansion test section of a wind tunnel. *Journal of Wind Engineering and Industrial Aerodynamics* **178**, https://doi.org/10.1016/j.jweia.2018.02.007 (2018).
44. Bruun, H. H., Khan, M. A., Al-Kayiem, H. H. & Fardad, A. A. Velocity calibration relationships for hot-wire anemometry. *Journal of Physics E: Scientific Instruments* **21**, 225–232, https://doi.org/10.1088/0022-3735/21/2/020 (1988).
45. Attenborough, K. In: Springer Handbook of Acoustics Part A. (ed. Rossing, T.), Ch 4, https://doi.org/10.1007/978-0-387-30425-0_4 (Springer, 2007).

46. He, R., Sun, H., Gao, X. & Yang, H. Wind tunnel tests for wind turbines: A state-of-the-art review. *Renewable and Sustainable Energy Reviews* **166**, 112675, https://doi.org/10.1016/j.rser.2022.112675 (2022).
47. Moffat, R. J. Describing the Uncertainties in Experimental Results. *Experimental Thermal and Fluid Science* **1**, 3–17, https://doi.org/10.1016/0894-1777(88)90043-X (1988).
48. Pagnini, L., Freda, A. & Piccardo, G. Uncertainties in the evaluation of one degree-of freedom galloping onset. *European Journal of Environmental and Civil Engineering* **21**(7-8), 1043–1063, https://doi.org/10.1016/j.engstruct.2021.112587 (2017).
49. Tubino, F., Pagnini, L. & Piccardo, G. Uncertainty propagation in the serviceability assessment of footbridges. *Structure and Infrastructure Engineering* **16**(1), 123–137, https://doi.org/10.1080/15732479.2019.1618879 (2020).
50. Keum, S. J., Jun, I. J., Pan, J. K. & Ryu, K. W. Effects of end plates with various shapes and sizes on helical Savonius wind turbines. *Renewable Energy* **79**, 167–176, https://doi.org/10.1016/j.renene.2014.11.035 (2015).
51. Ricci, R., Romagnoli, R., Montelpare, S. & Vitali, D. Experimental study on a Savonius wind rotor for street lighting systems. *Applied Energy* **161**, 143–152, https://doi.org/10.1016/j.apenergy.2015.10.012 (2016).
52. Talukdar, P. K., Sardar, A., Kulkarni, V. & Saha, U. K. Parametric analysis of model Savonius hydrokinetic turbines through experimental and computational investigations. *Energy Conversion and Management* **158**, 36–49, https://doi.org/10.1016/j.enconman.2017.12.011 (2018).
53. Al-Gburi, K. A. H., Alnaimi, F. B. I., Al-quraishi, B. A., Sann Tan, E. & Maseer, M. M. A comparative study review: The performance of Savonius-type rotors. *Materials Today: Proceedings* **57**, 343–349, https://doi.org/10.1016/j.matpr.2021.09.226 (2022).
54. Blackwell, B. F., Sheldahl, R. E. & Feltz, L. V. Wind tunnel performance data for two and three-bucket Savonius rotors. SAND 76-0131:1–105 (Sandia Laboratories, 1977).
55. Ross, I. & Altman, A. Wind tunnel blockage corrections: Review and application to Savonius vertical-axis wind turbines. *Journal of Wind Engineering and Industrial Aerodynamics* **99**(5), 523–538, https://doi.org/10.1016/j.jweia.2011.02.002 (2011).
56. Roy, S. & Saha, U. K. An adapted blockage factor correlation approach in wind tunnel experiments of a Savonius-style wind turbine. *Energy Conversion and Management* **86**, 418–427, https://doi.org/10.1016/j.enconman.2014.05.039 (2014).
57. Barlow, J. B., Rae, W. H. & Pope, A. *Low-speed wind tunnel testing* (John Wiley & Sons, 1999). https://doi.org/10.1201/9780367814908

Acknowledgements

This work is part of the transnational access project "THRUST", supported by the Engineering Research Infrastructures for European Synergies (ERIES) project (www.eries.eu), which has received funding from the European Union's Horizon Europe Framework Programme under Grant Agreement No. 101058684. This is ERIES publication number D7.

Author contributions

Luisa Pagnini: Data curation, Database analysis, Validation, Writing – original draft & editing. Piotr Doerffer: Conceptualization, Wind tunnel tests, Methodology, Co-supervision. Joanna Grzelak: hot wire measurements. Józef Kotus: sound measurements and preparation of the corresponding data set. Giuseppe Piccardo: Co-supervision, Writing – review & editing. Maria Pia Repetto: Funding. Krzysztof Doerffer: Conceptualization, Wind tunnel experiments, Methodology, Supervision. He is the PI of this research project.

Competing interests

The authors declare no competing interests.

Additional information

Correspondence and requests for materials should be addressed to L.P.

Reprints and permissions information is available at www.nature.com/reprints.

Publisher's note Springer Nature remains neutral with regard to jurisdictional claims in published maps and institutional affiliations.